Bioactive Materials 7 (2022) 491–503

Contents lists available at ScienceDirect

Bioactive Materials

journal homepage: www.sciencedirect.com/journal/bioactive-materials

An enamel-inspired bioactive material with multiscale structure and antibacterial adhesion property

Hai Ming Wong [a,*], Yu Yuan Zhang [a], Quan Li Li [b,**]

[a] Paediatric Dentistry and Orthodontics, Faculty of Dentistry, The University of Hong Kong, 34 Hospital Road, Hong Kong
[b] Collage and Hospital of Stomatology, Anhui Medical University, No. 69, Meishan Road, Heifei, China

ARTICLE INFO

Keywords:
Biomimetic mineralization
Enamel-inspired material
Bioactive material
Graphene oxide
Enamel-like structure

ABSTRACT

Conventional dental materials lack of the hierarchical architecture of enamel that exhibits excellent intrinsic-extrinsic mechanical properties. Moreover, restorative failures frequently occur due to physical and chemical mismatch between artificial materials and native dental hard tissue followed by recurrent caries which is caused by sugar-fermenting, acidogenic bacteria invasion of the defective cite. In order to resolve the limitations of the conventional dental materials, the aim of this study was to establish a non-cell-based biomimetic strategy to fabricate a novel bioactive material with enamel-like structure and antibacterial adhesion property. The evaporation-based, bottom-up and self-assembly method with layer-by-layer technique were used to form a large-area fluorapatite crystal layer containing antibacterial components. The multilayered structure was constructed by hydrothermal growth of the fluorapatite crystal layer and highly conformal adsorption to the crystal surface of a polyelectrolyte matrix film. Characterization and mechanical assessment demonstrated that the synthesized bioactive material resembled the native enamel in chemical components, mechanical properties and crystallographic structure. Antibacterial and cytocompatibility evaluation demonstrated that this material had the antibacterial adhesion property and biocompatibility. In combination with the molecular dynamics simulations to reveal the effects of variables on the crystallization mechanism, this study brings new prospects for the synthesis of enamel-inspired materials.

1. Introduction

Dental enamel is the hardest mineralized tissue in human bodies. It owns the hierarchical structure ranges from the nano-to macroscopic scale, arising from precisely controlled crystal nucleation and growth [1]. This distinctive hierarchical structure makes native enamel be characterized by its outstanding esthetic appearance and intrinsic-extrinsic fracture-toughening mechanisms [2]. Apart from improved mechanical properties [3], artificial materials with an ordered hierarchical structure have superior biocompatibility to those with randomly oriented structures [4,5]. In the context of dental restoration, failures, such as fracture and marginal leakage, are common due to the physical and chemical mismatch between artificial materials and native dental hard tissue [6]. In addition, food debris easily accumulates on the surface of conventional tooth colored materials to generate dental plaque-retentive sites most commonly at the interface between the restoration and the cavity prepared, followed by the invasion of cariogenic bacteria, mainly Streptococcus mutans (S. mutans) [7,8]. This results in recurrent caries and subsequent dislodge of the restoration, and leads to the vicious cycle of re-restoration with increasing size that ultimately shortens the tooth's life expectancy. It was reported that more than half of the restorations placed in the United States in 2005 were replacements of failed restorations [9]. Hence, there is growing interest in synthesizing dental restorative materials that have distinctive hierarchical architecture in native enamel and exhibit antibacterial properties.

Inspired by the process of amelogenisis, the reconstruction of a highly organized structure may be achieved by the addition of organic matrices which mediate crystal growth and form hierarchical structures, whereby assembly is based on tunable organic-inorganic interactions [10]. Examples of non-protein based organic matrices used in enamel biomineralization include citrate [11], surfactant [12], triethylamine

Peer review under responsibility of KeAi Communications Co., Ltd.
* Corresponding author. Paediatric Dentistry and Orthodontics, Faculty of Dentistry, The University of Hong Kong, 34 Hospital Road, Hong Kong.
** Corresponding author. Collage and Hospital of stomatology, Anhui Medical University, No. 69, Meishan Road, Heifei, China.
E-mail addresses: wonghmg@hku.hk (H.M. Wong), u3004976@connect.hku.hk (Y.Y. Zhang), ql-li@126.com (Q.L. Li).

https://doi.org/10.1016/j.bioactmat.2021.05.035
Received 17 February 2021; Received in revised form 21 May 2021; Accepted 24 May 2021
Available online 2 June 2021

[13], glycerine and gelatine [14], self-assembling monolayers [15], and agarose hydrogels [16]; while protein-based organic matrices include peptide amphiphiles with the Arg-Gly-Asp (-RGD) motif [17], amelogenin in the presence of fluoride [18], amelogenin-chitosan hydrogels [19], and elastin-like recombinamers [20]. Although previous studies synthesized enamel-like nano- and microstructures [11–20], and even enamel-inspired films [21,22], none of these previous attempts have successfully recreated native enamel's complex hierarchical prism and interprismatic structures. Regarding strategies for breaking the vicious cycle of re-restoration, antibacterial agents such as fluoride, chlorohexidine, and metal particles have been added into conventional dental materials to prevent recurrent caries. Unfortunately, the incorporation of antibacterial agents led to deteriorated mechanical properties of the synthesized materials [23], and their antimicrobial effects varied [24].

The aim of this study was to synthesize a novel macroscopic bioactive material with the enamel-like structure and antibacterial adhesion property. We intended to use the layer-by-layer (LBL) deposition technique to control crystallization process and self-assembly of synthesized crystals. The LBL deposition technique is a versatile nanoscale approach, which uses alternately anionic polyelectrolyte and cationic polyelectrolyte to form a matrix film. The technique has been widely used to construct ordered layers of materials for use in fields including optics, energy, catalysis, separations, and biomedicine [25,26]. Recently, Yeom et al. synthesized ZnO columnar nanocomposites with well-defined morphologies and patterns and a multilayered structure via the bottom-up LBL deposition of a polymeric matrix [21]. There is also evidence that evaporating the mineralization solution could speed up the process of crystal growth and help crystals self-assemble into oriented arrays [27,28]. Therefore, the evaporation-based, bottom-up and self-assembly method with LBL technique were used in the present study. We further introduced graphene oxide (GO) into the LBL organic matrix film to impart the antibacterial adhesion property to the synthesized bioactive material without weakening its mechanical characteristics. GO is a chemically modified graphene with reactive carboxylic acid and hydroxyl moieties. GO has antibacterial abilities via the mechanism of oxidative stress produced by radical oxygen species to interfere with bacterial metabolic activity and inactivate bacteria [29]. Because the chemical cross-linking of reactive carboxylic acid and hydroxyl moieties in GO gives it excellent mechanical properties [30], GO has been used in the synthesis of calcium phosphate-based materials for strengthening and toughening hydroxyapatite (the major inorganic component of native enamel) crystals [31]. Moreover, fluorapatite is more acid- and caries-resistant than hydroxyapatite [32] so that fluoride was added into the mineralization solution in order to form fluorapatite crystals rather than hydroxyapatite crystals. The ultimate strategy we proposed was using polyanionic electrolyte (GO/alginate) and polycationic electrolyte (chitosan) LBL polyelectrolyte complex film to regulate fluorapatite crystals self-assembling into the enamel-like structure on a dissolvable polydopamine and polyethylene base under evaporation.

2. Methods and materials

2.1. Preparation of the dissolvable mineralization base for LBL deposition

Commercially available polyethylene plates were cut into an appropriate size (diameter = 50 mm), polished with 1500-grit silicon carbide paper, and orderly cleaned with acetone, ethanol, and deionized water. For each solvent, the samples were ultrasonically treated for 5 min. A total of 3 times of repeated clean cycles were proceeded. The polished polyethylene plates were then immersed in a freshly prepared 2 mg/mL polydopamine solution (Sigma-Aldrich, St. Louis, MO) (1.21 mg/mL Tris buffer, pH 8.5) at 37 °C in the dark for 24 h. The plates were subsequently sonicated for 10 min in deionized water three times to remove the nonattached polydopamine, before being dried under nitrogen gas at 37 °C. The obtained polydopamine-coated polyethylene plates were stored in deionized water at 4 °C before use.

2.2. Preparation of polyelectrolyte matrices for LBL deposition

Two types of polyelectrolyte matrices were prepared for LBL deposition, namely polyelectrolyte matrix A (0.1 wt% GO or 0.1 wt% alginate) and B (0.1 wt% chitosan).

Synthesis of GO and preparation of GO solution. GO was synthesized by pyrolyzing citric acid. 1 g citric acid (Sigma-Aldrich, St. Louis, MO) was put into a 5 mL beaker and heated to 200 °C using a heating mantle (S88854105, Hot Plate Magnetic Stirrer, Cimarec+™ Stirrer Series; Thermo Scientific™). Citric acid was liquefied after 5 min, and its color changed from colorless to yellow. Its color changed to orange in 30 min. The heating was kept until it changed into black liquid in 100 min, suggesting the formation of graphene oxide. The obtained black liquid was mixed with deionized water and adjusted by 10 mg/mL NaOH solution to obtain 0.1 wt% GO solution with pH 5.5 [33].

Preparation of chitosan and alginate solutions. 0.5 g chitosan (low molecular weight; Sigma-Aldrich, St. Louis, MO) was dissolved in 0.17 mM acetic acid solution, being adjusted by 10 mg/mL NaOH solution to obtain 0.1 wt% chitosan solution with pH 5.5.0.5 g alginate (Sigma-Aldrich, St. Louis, MO) was dissolved in deionized water, being adjusted by 36.5 mg/mL HCL solution to obtain 0.1 wt% alginate solution with pH 5.5.

2.3. Fabrication of the enamel-inspired bioactive material

The bioactive material was fabricated by repeated, alternate treatment cycles of mineralization and LBL deposition, as described below.

Evaporation-based, bottom-up and self-assembly mineralization process. Polydopamine-coated polyethylene plates were floated in a metastable calcium phosphate mineralization solution with the addition of ethylenediaminetetraacetic acid (EDTA) (1.0 L mineralization solution: 7.9 g NaCl, 64.4 mg $CaCl_2$, 49.6 mg Na_2HPO_4, 4.9 mg NaF, 17.0 g EDTA, pH 5.5) or a metastable calcium phosphate mineralization solution without EDTA (1.0 L mineralization solution: 7.9 g NaCl, 64.4 mg $CaCl_2$, 49.6 mg Na_2HPO_4, 4.9 mg NaF, pH 5.5), and heated in an oven (DO120; DragLab Technologies) at 70 °C for 7 days. Fresh mineralization solution was added every three days to prevent from complete evaporation.

LBL deposition. After mineralization, the plates were rinsed with deionized water and dried in a vacuum desiccator (133 Pa, 37 °C; DZF-6050; YIHENG Technical Co., Ltd.). LBL deposition was then carried out as the following procedures. The dried sample was alternately immersed in freshly prepared polyelectrolyte matrix A and B in a vacuum chamber (133 Pa, 37 °C; DZF-6021; YIHENG Technical Co., Ltd.) for 10 min. The sample was thoroughly rinsed with deionized water between immersions. Each polyelectrolyte matrix film was assembled after a total of 10 repeated switches of polyelectrolyte matrixes (10 immersions in matrix A and 10 immersions in matrix B).

Isolation of the enamel-inspired bioactive material. After eight treatment cycles, the samples were immersed in the isoamyl acetate solution to dissolve the polyethylene plates. The synthesized bioactive material was then isolated from the mineralization base. The obtained material was then characterized.

2.4. Characterization

Scanning electron microscopy (SEM). SEM analysis was conducted on a Carl Zeiss Supra 40 field emission scanning electron microscope (2–5 kV, depending on the sample state). The SEM samples were coated with Au film using a benchtop sputter coater (COLDCOATER, LUXOR™) for 30 s at a constant current of 30 mA before observation.

Energy Dispersive Spectroscopy (EDS). EDS data were acquired using EDS spectroscopy (Hitachi S4800, Hitachi Ltd., Tokyo, Japan; FEI, Sirion 200, USA). The selected area was located in the center of each specimen, and the size was 200 μm by 200 μm.

High-resolution transmission electron microscopy (HRTEM). A JEOL 3011 high resolution electron microscope (JEOL USA, Peabody, MA, USA) operating at 300 kV was used for HRTEM analysis to inspect the crystallographic features of the synthesized material.

Fourier transform infrared spectroscopy (FTIR). Infrared spectra of samples between 4000 cm^{-1} to 400 cm^{-1} were acquired by a Thermo Scientific Nicolet 8700 F T-IR spectrometer in attenuated total reflectance mode. Samples were prepared by coating polyelectrolyte matrix solution on the surface of the fluorapatite crystal layer to detect the existence of formed polyelectrolyte matrix films and their cross-linkage.

X-ray diffraction. XRD data were measured by a PANalytical X'pert PRO MRD X-ray diffractometer equipped with Cu Kα radiation (λ = 1.54056 Å). X-ray diffractometer was operated at 45 kV and 40 mA. A scan speed of 2°/min was employed over the angular range from 3° to 60° in 2θ.

Confocal laser scanning microscopy (CLSM). The cell morphology of human gingival fibroblasts (HGF-1, ATCC CRL-2014) adhered on samples was illustrated by CLSM (Fluoview 1000, Olympus).

Thermogravimetric analysis (TGA). TGA data (in air) were measured with a TA Instruments SDT Q600 thermogravimetric analyzer. Samples were ground into powders, placed in a Al_2O_3 pan and heated at a rate of 30 °C/min to 800 °C in air. The data were analyzed using the Universal Analysis 2000 software and expressed as weight vs temperature, and each sample group was repeated five times (n = 5).

2.5. Mechanical evaluation

Microhardness test. All samples were dehydrated with the process of gradient ethanol dehydration (50% × 1 time, 70% × 1 time, 80% × 1 time, 90% × 1 time, 95% × 1 time, and 100 % × 3 times; each step for 15 min). The mechanical properties were evaluated through a microhardness tester (Leica DC 300, Leitz, Germany). Before testing, the tester was calibrated with a standard calibration reference block. A stage micrometer was placed on the anvil, and the instrument's measuring lines were placed at a known distance on the stage micrometer. This distance was then compared to the unit's measuring system. If they did not agree, the ocular was moved in/out to increase/decrease the measuring distance. The samples were then subjected to microhardness tester with a load of 25 g (0.245 N) for 20 s. For each sample, 10 test points with 30 mm spacing on the sample surface were evaluated.

Nanoindentation test. The elastic modulus and nanohardness of the synthesized bioactive material were evaluated by Nanoindentation measurement (TI900 Nanomechanical Test Instrument, Hysitron Inc.). The times of loading and unloading were both 15 s, and the holding time was 10 s under the maximum applied force of 40 mN. Six sites were tested for each sample. The elastic modulus and nanohardness were calculated from the force-displacement curves by using the Triboscan Quasi software. The native enamel slices were used as the control group.

All the obtained data were recorded and analyzed with statistical software (SPSS Statistic 25; IBM). Differences were considered significant at $p < 0.05$ (*t*-test). Data were expressed as mean ± standard deviation.

2.6. Antibacterial adhesion evaluation

The colony forming units (CFU) counting method was applied to evaluate the antibacterial adhesion ability of the bioactive material. Synthesized materials (with a chitosan-alginate matrix: n = 10; and with a GO-chitosan matrix: n = 10) and enamel slices (n = 10) with a size of 3*3*1.5 mm^3 were prepared and autoclave sterilized at 121 °C for 60 min (SSR-3A; Consolidated Sterilizer System, CSS). Samples were immersed in the artificial saliva (0.33 g KH_2PO_4, 0.34 g Na_2HPO_4, 1.27 g KCl, 0.16 g NaSCN, 0.58 g NaCl, 0.17 g $CaCl_2$, 0.16 g NH_4Cl, 0.2 g urea, 0.03 g glucose, 0.002 g ascorbic acid, 2.7 g mucin in 1000 mL distilled water; pH 7) overnight. S. mutans (ATCC 35668, ATCC, Manassas) cells were cultured in Horse Blood Medium (HBI; 31.2 g Columbia agar base, 800 mL distilled water, 40 mL horse blood, 0.1 g hemin, 0.08 g NAOH, 200 mL distilled water) under anaerobic condition (85% N_2, 10% H_2, and 5% CO_2) at 37 °C in an anaerobic chamber (Forma Anaerobic Chamber; Thermo Fisher Scientific, Inc). Cells were harvested by centrifugation (5000 rpm, 10 min), washed once with 10 mM sodium phosphate-buffered saline (PBS, pH 7.2), and resuspended in brain-heart infusion broth (BHI, Difco Laboratories, Detroit) at a concentration of 10^6 CFU/mL. Samples were horizontally placed at the bottom of a 96-well plate with the addition of 200 μL of S. mutans in BHI (10^6 CFU/mL).

After incubation under anaerobic condition at 37 °C for 24 h, samples were rinsed three times with PBS, placed in 1 mL fresh BHI solution, and then treated by sonication for 60 s to collect the adherent bacteria from the sample surfaces. The procedures were operated in a horizontal laminar flow clean bench (Polypropylene Horizontal Laminar Flow Clean Bench; AirClean 5000 Workstation, AirClean Systems). Ten-fold serial dilutions of the bacterial suspensions were plated in duplicate on horse blood agar. After a 48-h incubation, CFU was counted. Three independent biofilm experiments were performed.

2.7. Cytocompatibility evaluation

HGF-1 cells were obtained from the American Type Culture Collection, which was used to test the biosecurity of the fabricated biomaterial. HGF-1 cells were cultured in high glucose Dulbecco's modified Eagle's medium (DMEM; Sigma-Aldrich) supplemented with 4 mM L-glutamine (Sigma-Aldrich) and 10% (vol/vol) heat-inactivated fetal bovine serum (FBS; Sigma-Aldrich). No antibiotic supplement was used. Cells were incubated at 37 °C in a 5% CO_2 atmosphere, fed every 48 h and routinely sub-cultured every 5 days with a split ratio of 1:3 using 1 × trypsin-EDTA (0.05%; Sigma-Aldrich) for 3 min at 37 °C.

Cell viability assay. The synthesized bioactive materials (with a chitosan-alginate matrix: n = 10; and with a GO-chitosan matrix: n = 10) and enamel slices (n = 10) with a size of 3*3*1.5 mm^3 were prepared. After autoclave sterilization, samples were placed into a 96-well plate and soaked with 1 mL cell suspension (6.0*10^3 cells/well) in a 5% CO_2 incubator at 37 °C for 7 days. A Cell Counting Kit-8 (CCK-8; Dojindo Molecular Technology, Kumamoto, Japan) was used to quantitatively evaluate the cell viability of samples by dying living cells. After 4 h' incubation at 37 °C, the resultant production of water-soluble formazan dye was assayed at a wavelength of 450 nm by a microplate reader (Multiscan MK3; Thermo Fisher Scientific, Inc).

Fluorescence assays. Synthesized bioactive materials (with a chitosan-alginate matrix: n = 6; and with a GO-chitosan matrix: n = 6) and enamel slices (n = 6) with similar size were prepared. After autoclave sterilization, samples were placed into a 96-well plate and soaked with 1 mL cell suspension (6.0*10^3 cells/well) in a 5% CO_2 incubator at 37 °C. At the end of 7 days, samples were removed and placed in a new 96-well plate, and incubated with CellTracker™ Green CMFDA (C7025, Thermo Fisher Scientific, Waltham) at 37 °C for 30 min. After removing the stain solution, samples were washed with PBS.

2.8. Molecular dynamics (MD) simulation

All the molecules were prepared in Chemdraw16.0, B3LYP/6-31G* by Gaussian09 program and the TIP3P model [34–36]. The tleap program in Amber16 was applied to construct the molecule system. Molecular dynamics simulations were run using the openMM MD package [37]. The simulations were carried out in multiple steps. First, the whole system was miniaturized, particularly for the water molecules. After that, the Langevin thermostat [38] was applied to heat the system to 330 K. The NPT ensemble was used to equilibrate the system to a pressure of 1 atm. Finally, long-time MD simulations (100 ns) were run under the NVT ensemble. The Shake algorithm [39] was applied to constrain the movement of bonded hydrogen. The HF/6-31G* method and basis set was used to calculate the electrostatic potential (ESP) and the result was used to calculate the restricted ESP (RESP)[2] of the

molecules [40]. The geometric properties of the molecules were described using the general amber force field (gaff) [41].

3. Results and discussion

The multiscale, macroscopic bioactive material was obtained in this study. This bioactive material was synthesized on a dissolvable mineralization base via the evaporation-based, bottom-up and self-assembly method in conjunction with the LBL technique. Its schematic fabrication process is illustrated in Fig. 1A. A customized mineralization template was used to synthesize enamel-like fluorapatite crystals under a hydrothermal condition. The LBL technique was then introduced to form the polyelectrolyte matrix film in order to induce epitaxial overgrowth of original crystals, generate new crystals, eliminate crystal voids and fabricate a large-area fluorapatite crystal layer. The multilayered fluorapatite crystal material was constructed by repeated treatment cycles, and finally isolated by dissolving the mineralization base. SEM images of the bioactive material with one, two, and multiple crystal layers are shown in Fig. 1B.

3.1. Synthesis of enamel-like fluorapatite crystals

The crystals in native enamel have a cross-section diameter of 25–100 nm and a length of 100 nm–100 μm or longer along the *c*-axis (Fig. 2A). At pH 5.5, enamel-like fluorapatite crystals were synthesized with the addition of EDTA. They had a spear-like morphology with a cross-section diameter of 69–109 nm and a length of 600 nm-11.2 μm along the *c*-axis (Fig. 2B and C). The selected-area electron diffraction (SAED) micrograph had an arc-like pattern, indicative of the typical crystal structure of enamel (Fig. 2D) [42].

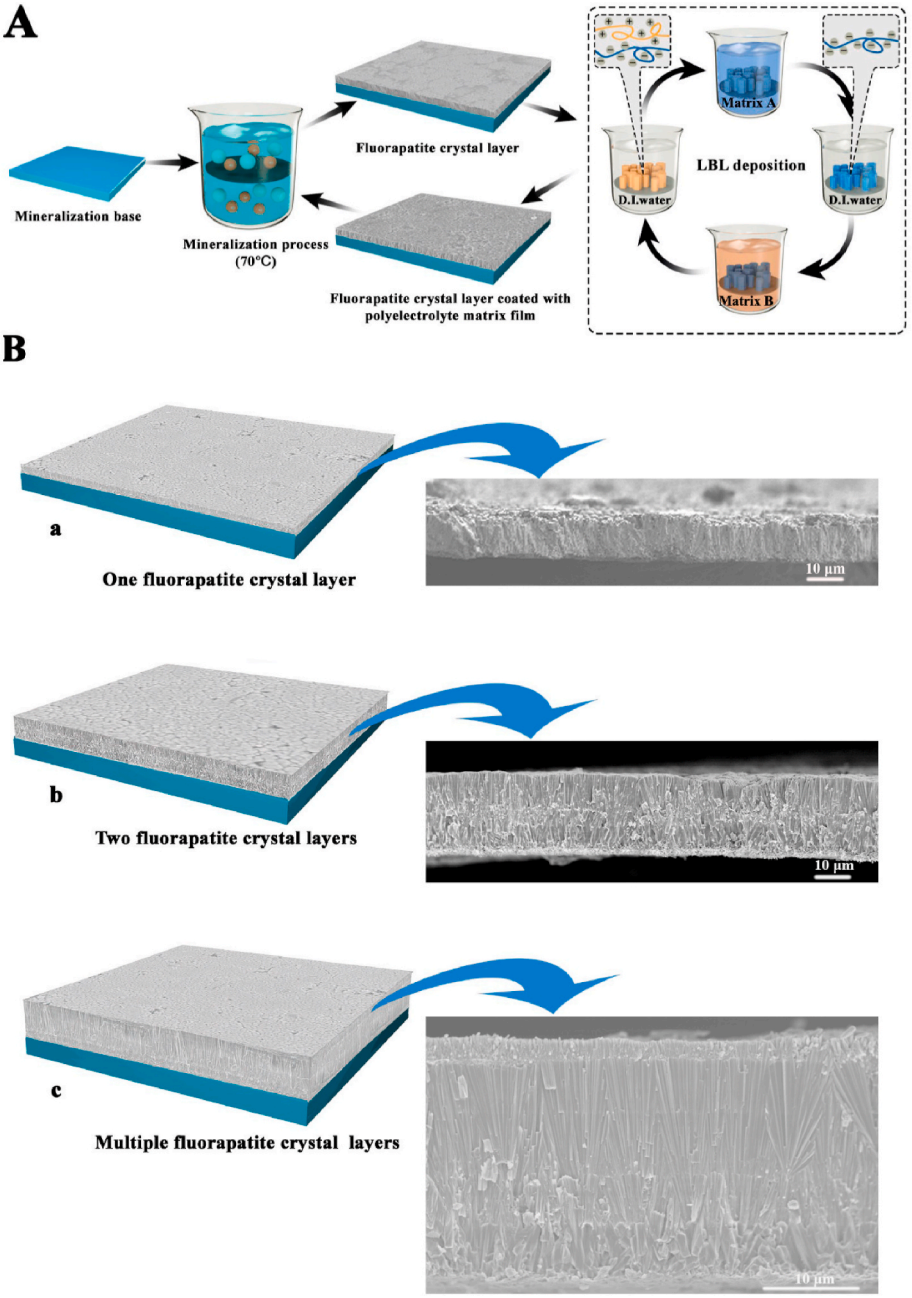

Fig. 1. (A) Fabrication process of the bioactive material. (B) Scanning electron microscopy (SEM) images of the bioactive material with (a) one, (b) two, and (c) multiple crystal layers.

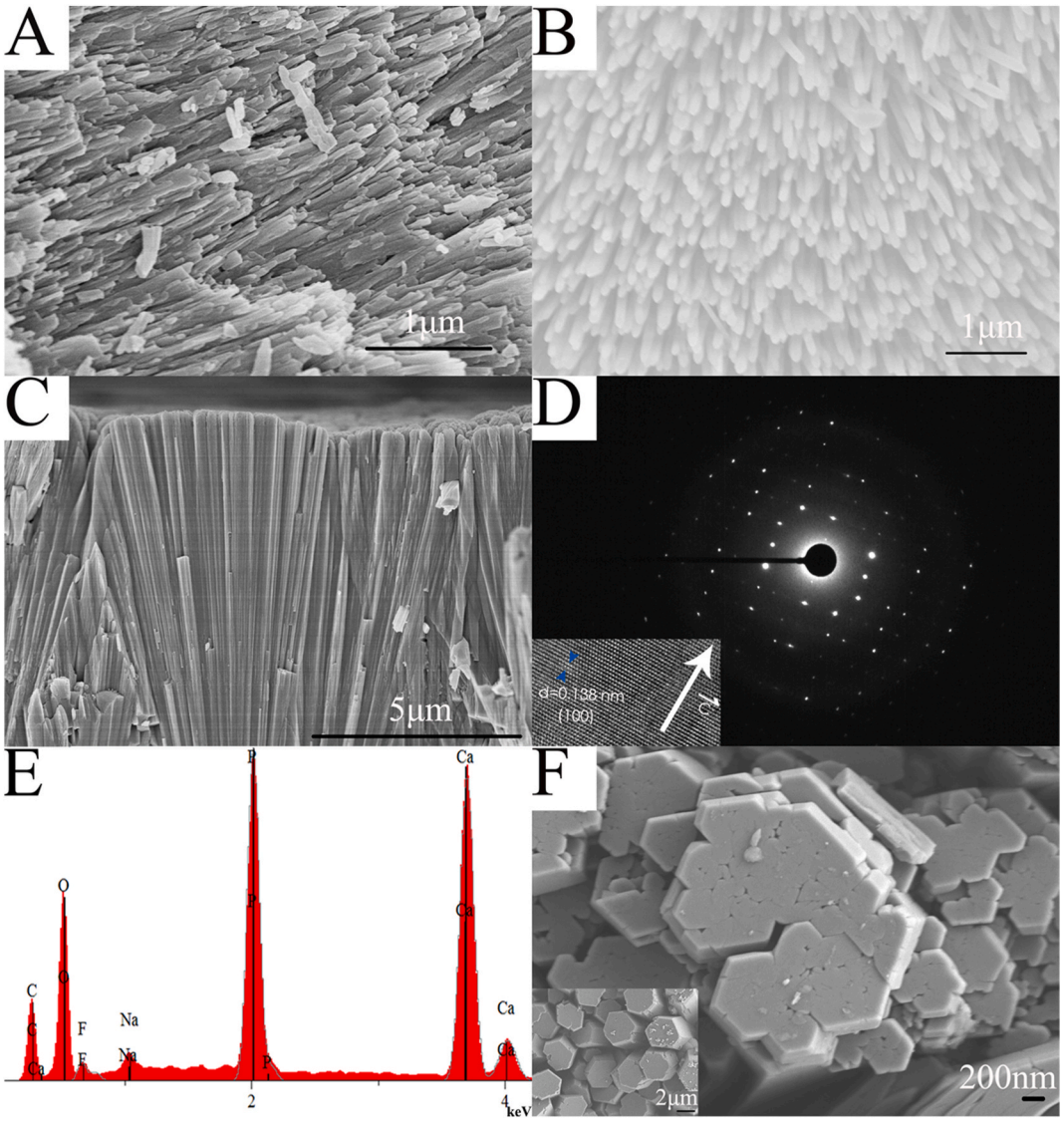

Fig. 2. (A) Scanning electron microscopy (SEM) image of native enamel. SEM images (B, C), high-resolution transmission electron micrograph (D), and energy-dispersive X-ray spectrum (E) of fluorapatite crystals synthesized with the addition of ethylenediaminetetraacetic acid (EDTA). (F) SEM image of hexagonal fluorapatite crystals synthesized without EDTA (a magnified micrograph is shown in the inset).

The HRTEM micrograph showed a regular spacing of 0.138 nm of the observed lattice plane (Fig. 2D, inset). The SEM results identified a high similarity in morphology and size between the synthesized fluorapatite and native enamel. Besides, EDS analysis demonstrated the existence of fluoride in the formed crystals, and an average Ca/P molar ratio of 1.64 ± 0.04 (n = 10; Fig. 2E), resembling that of stoichiometric hydroxyapatite in enamel (1.67 ± 0.02; n = 10, $p = 0.192$, *t*-test) (Supplementary Fig. 1). By contrast, in the absence of EDTA, hexagonal fluorapatite crystals formed by the parallel aggregation of nanorod-like crystals (Fig. 2F). The cross-section diameter of these crystals was 2–5 μm, which is larger than that in enamel.

We used a metastable calcium phosphate mineralization solution with fluoride because fluoride ions mediate mineral growth by occupying the hydroxyl site in the long *c*-axis of the crystal [43]. In addition, fluorapatites are more acid-resistant than non-fluoridated crystals [32].

During the mineralization process, free Ca^{2+} ions in the metastable mineralization solution were captured and deposited on the mineralization base to form nucleation sites for mineral growth and crystal formation. This was enabled by the electrostatic interaction between Ca^{2+} with the phenol groups of polydopamine.

3.2. Fabrication of the enamel-like fluorapatite crystal layer

3.2.1. LBL deposition

After the initial evaporation-based, bottom-up and self-assembly mineralization process, the formed crystals had a loose interior structure, owing to the abundance of microscale voids (Fig. 3A and B). This resulted in the crystals falling off the mineralization base on the seventh day of the mineralization process, breaking into small patches, which were too brittle to be picked up with tweezers. This restricted the fabrication of a large-area fluorapatite crystal film. Pure calcium phosphate cannot be used in load-bearing devices, because of its inferior wear resistance and fracture toughness [44]. Native enamel is composed of more than 95% inorganic material and less than 5% organic matrix by weight [45]. The soft organic matrix in enamel is interlaced with nanoscale crystals, and participates in the assembly of crystals into crystal prisms. These crystals and prisms interlace together to support the enamel against external loads [46]. In addition, the manner in which the mineral phase and the organic material are organized can give rise to isotropic properties from inherently anisotropic components, which is the key factor contributing to the distinctive mechanical properties in biomaterials [47]. Thus, we used LBL deposition to introduce the

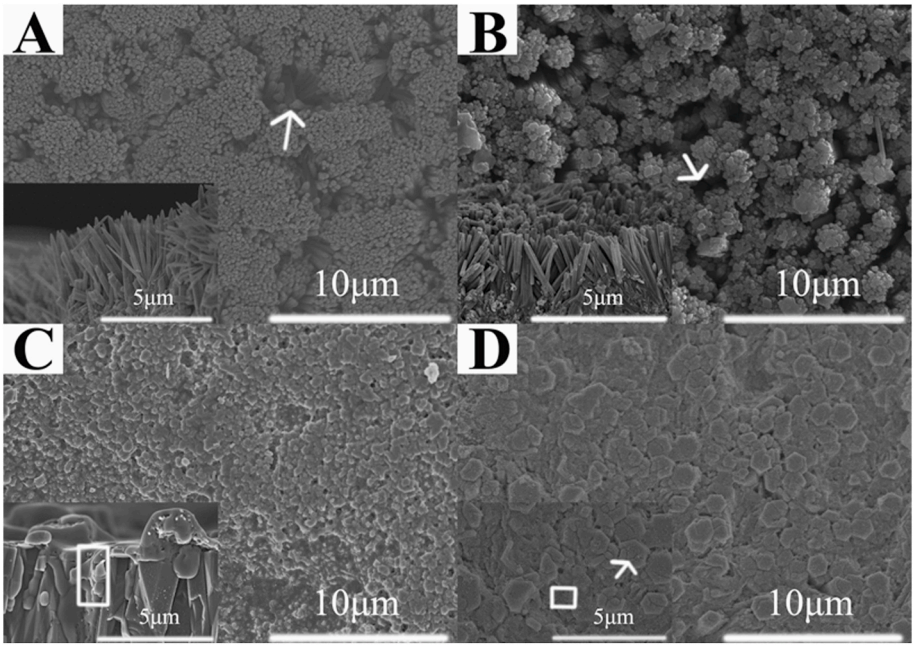

Fig. 3. Scanning electron microscopy evaluation of fluorapatite crystals formed before and after layer-by-layer (LBL) deposition. (A) Top-view micrograph of spear-like fluorapatite crystals synthesized with the addition of ethylenediaminetetraacetic acid (EDTA) before LBL deposition (the arrow represents the crystal voids; the inset is the transversal-view micrograph). (B) Top-view micrograph of hexagonal fluorapatite crystals synthesized without the addition of EDTA before LBL deposition (the arrow represents the crystal voids; the inset is the transversal-view micrograph). (C) Top-view micrograph of fluorapatite crystals coated with the polyelectrolyte matrix film (inset is the transversal-view micrograph; the rectangle in the inset indicates where the polyelectrolyte matrix infiltrated into the crystal voids). (D) Top-view micrograph of fluorapatite crystals treated with LBL deposition after two days mineralization (the arrow in the inset indicates the mineralized polyelectrolyte matrix on the crystal surface; the rectangle in the inset represents where the mineralized polyelectrolyte matrix occupied the crystal voids).

organic matrix and to fabricate a large-area fluorapatite crystal layer with a hierarchal architecture. We achieved this by adsorbing the charged matrix onto the synthesized fluorapatite crystals, and then, after washing, absorbing an oppositely charged matrix on top of the first layer.

3.2.2. Formation of polyelectrolyte matrix film

After LBL deposition, fluorapatite crystals were coated with a layer of hydrophilic polyelectrolyte matrix film (Fig. 3C). FTIR was used to assess the cross-linking of chitosan and alginate in the polyelectrolyte matrix film. In the FTIR spectrum of chitosan (Fig. 4A), we observed a broad band at 3292.2 cm^{-1}, corresponding to NH_2 groups and –OH groups, and peaks at 2050.5 and 1031.8 cm^{-1}, corresponding to –OH stretching and C–O epoxide groups, respectively [46]. For the spectrum of alginate (Fig. 4B), the peaks at 1028.6 cm^{-1}, 1452.4 and 1601.4 cm^{-1} were assigned to the C–O–C stretching, and asymmetric and symmetric stretching in carboxylate groups [48]. After cross-linking with chitosan (Fig. 4C), the asymmetric stretching of $–COO^-$ groups in alginate shifted from 1601.4 to 1595.8 cm^{-1}, and the symmetric stretching of $–COO^-$ groups shifted from 1452.4 to 1412.7 cm^{-1} [49]. Additionally, the absorption band at 3292.2 cm^{-1} in chitosan shifted to 3285.2 cm^{-1} [50].

Chitosan and alginate both have excellent biocompatibility, biodegradation, antimicrobial activity, and low immunogenicity. The amino residues of chitosan electrostatically bind with the carboxylic residues of alginate to form a polyelectrolyte matrix film, which has been widely applied in tissue engineering, drug delivery and wound healing [51]. Chitosan cross-linked alginate was also used to synthesize bulk artificial nacre with good mechanical properties [52].

3.2.3. Epitaxial overgrowth of original crystals, formation of new crystals and elimination of voids

Under a vacuum environment, the hydrophilic polyelectrolyte matrix film infiltrated the crystal voids (Fig. 3C, inset) and planarized the crystal surfaces. Without the introduction of vacuum, plenty voids were detected in the fabricated fluorapatite crystal layer (Supplementary Fig. 2).

The polyelectrolyte matrix reacted with calcium and phosphate ions from the mineralization solution, and was mineralized (Fig. 3D). The mineralized polyelectrolyte matrix coated on the fluorapatite crystals in the growth stage induced epitaxial overgrowth of crystals and provided new nucleation sites to construct the next crystal layer (Fig. 3D; marked by the arrow in the inset). Within the voids, the matrix triggered the formation of new crystals, which then filled the voids (Fig. 3D; marked by the rectangle in the inset) [53,54].

3.2.4. Formation of a large-area fluorapatite crystal layer

On the fifth day of the mineralization process after LBL deposition, all voids in the crystal layer disappeared and were occupied by newly formed crystals (Fig. 5A and B), resulting in a large-area fluorapatite crystal layer.

Similar to the organic matrix in native enamel, the polyelectrolyte matrix interlaced with fluorapatite crystals, led to the epitaxial overgrowth of crystals, eliminated voids, joined neighboring crystals together to assemble into a prismatic structure, and formed a large-area fluorapatite crystal film. The microstructure in native enamel is composed of repeating units of crystal prisms. Each prism is made up of bundles of parallel oriented hydroxyapatite crystals along the *c*-axis [55]. These prismatic structures in the fluorapatite crystal layer (Fig. 5C) resemble those of native enamel (Fig. 5D).

3.3. Fabrication of the multilayered fluorapatite crystal material

After two treatment cycles, a continuous prismatic-type fluorapatite crystal material with the approximate thickness of 20–27 μm was synthesized, consisting of bundles of parallelly oriented fluorapatite crystals (Fig. 5E). The adjacent prismatic fluorapatite crystal layer was almost vertically oriented with respect to the underlying crystal film. Similar to that of native enamel (Fig. 5F(a)), the XRD spectra of the fluorapatite crystal layer showed strong characteristic diffraction peaks (002) at $2\theta = 25.8°$, (102) at $2\theta = 28.1°$, (211) at $2\theta = 31.8°$, (112) at $2\theta = 32.2°$, and (300) at $2\theta = 32.91°$ (Fig. 5F(b)). The peaks at (002) at $2\theta = 25.8°$ and (004) at $2\theta = 53.2°$ were distinct, which is indicative of the highly organized orientation in the fluorapatite crystal film, and is consistent with the transversal SEM image (Fig. 5E). In addition, the XRD patterns of the initial (Fig. 5F(b)) and second crystal layers showed the same orientation (Fig. 5F(c)), demonstrating that the newly formed crystal layer epitaxially matched the initial layer. This highly organized orientation is consistent with the prismatic microstructure in enamel [12].

In our previous study, we found that crystal growth was controlled

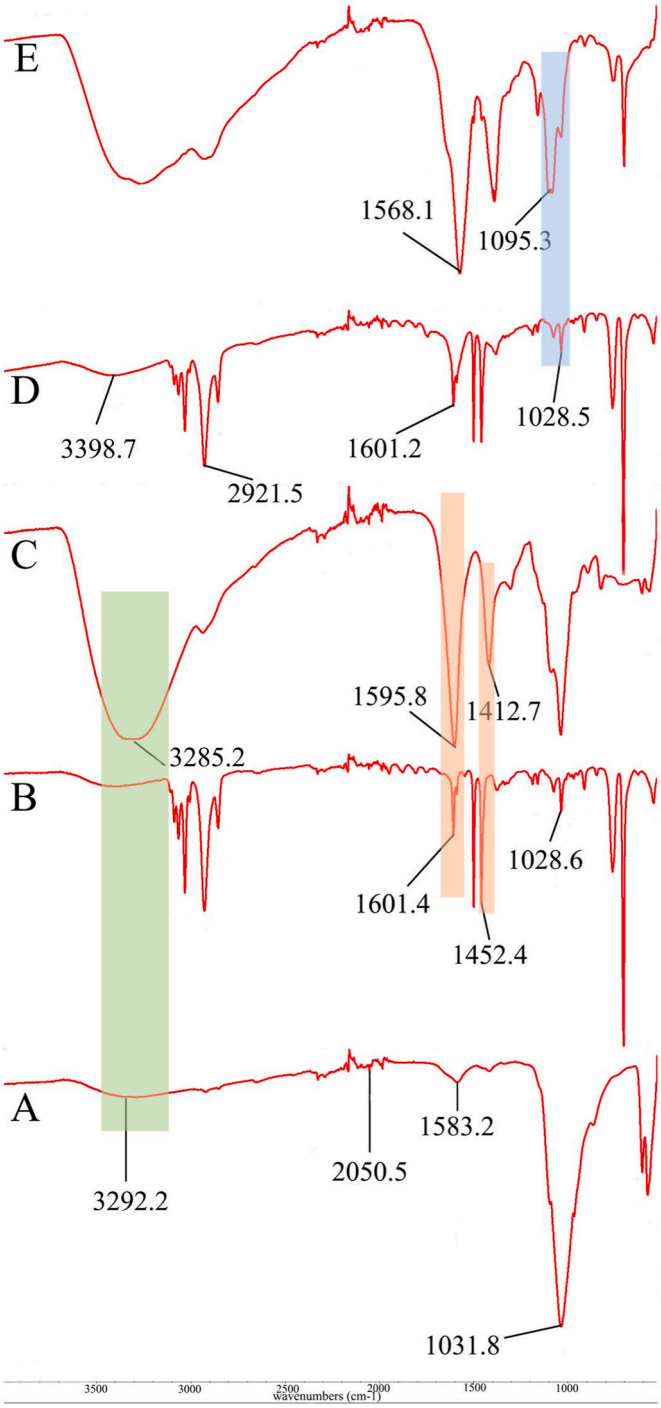

Fig. 4. Fourier-transform infrared spectra of formed polyelectrolyte matrix film. (A) Fluorapatite crystal layer coated with chitosan polyelectrolyte matrix film. (B) Fluorapatite crystal layer coated with alginate polyelectrolyte matrix film. (C) Fluorapatite crystal layer coated with chitosan cross-linked alginate polyelectrolyte matrix film. (D) Fluorapatite crystal layer coated with graphene oxide polyelectrolyte matrix film. (E) Fluorapatite crystal layer coated with graphene oxide cross-linked chitosan polyelectrolyte matrix film.

by the organic template and affected by the characteristics of the substrate surface [27]. In the present study, the first synthesized fluorapatite crystal layer grew on the polydopamine-coated polyethylene plate but the second crystal layer grew on the polyelectrolyte matrix film coated crystal layer. Thus, it is inevitable that different strengths of peak intensities were detected in these two layers (Fig. 5F), due to the difference in substrate surfaces. Although the substrate surface could regulate crystal nucleation, growth and orientation, it only participated in the initial stage of crystal formation [11]. The subsequent growth of crystals showed a preferred orientation along the c-axis, due to competition for the free available space between adjacent sites of growth; only crystals growing perpendicular to the surface of substrates had sufficient space to grow. Therefore, the final crystal orientation of a fabricated crystal layer would not be affected dominantly by the underneath substrate surface. Both the first and second fluorapatite crystal layers showed a strong intensity in the (002) plane, which indicated that the formed crystals had an oriented growth along the c-axis (Fig. 5F).

The thickness of the synthesized material could be controlled by the number of repeated treatment cycles (Fig. 6). The thickness of the isolated final material after eight cycles was approximately 81.5 μm (Fig. 6C).

The synthesized material was isolated by dissolving the mineralization base in an isoamyl acetate solution. Designing a removable mineralization base is crucial in this study to isolate and obtain the final synthesized bioactive material; however, it is methodologically challenging to produce such a removable epitaxial template [56–58]. We designed the removable mineralization base by combining polydopamine and polyethylene. Dopamine can self-polymerize into polydopamine to attract Ca^{2+}, providing nucleation sites and facilitating the growth of hydroxyapatite. In addition, its amine and phenol groups have the universal adhesive property to covalently or noncovalently bind with organic and inorganic compounds [59]. Polyethylene was used because it can be dissolved by isoamyl acetate at room temperature and is beneficial to the parallel growth of aligned hydroxyapatite crystals [60].

3.4. Synthesis of the bioactive material with antibacterial adhesion property

The characteristic peaks in the FTIR spectrum of the GO were located at 3398.7, 2921.5, 1601.2, and 1028.5 cm^{-1}, representing the stretching of –OH groups, C–H groups, C═O carbonyl stretching, and stretching of C–O epoxide groups, respectively (Fig. 4D). These are the main functional groups in GO [61,62]. The FTIR spectrum of the GO–chitosan film showed stretching vibrations of NHCO at 1568.1 cm^{-1}, which was generated by the reaction between the amino groups in chitosan chains with the carboxylic acid groups in GO (Fig. 4E) [66]. After cross-linking with chitosan, the peak of the C═O carbonyl stretching at 1601.2 cm^{-1} in GO disappeared (Fig. 4E) [63,64]. The peak of the C–O epoxide group stretching at 1095.3 cm^{-1} in the GO-chitosan film was more intense than that of GO (1028.5 cm^{-1}), which was caused by the epoxy–amino reaction. In chitosan, there was a dominant stretching band for primary amide groups (NH_2) at 1583.2 cm^{-1} (Fig. 4A); in GO-chitosan, this was replaced by a band at 1568.1 cm^{-1}, attributed to stretching of secondary amine groups and indicating the presence of newly formed amide bonds in the GO-chitosan film (Fig. 4E) [65]. Ca^{2+} ions can tightly bind to carboxylic acid groups at the edges of individual GO, and to oxygen functional groups in GO, causing sliding by cross-linking of neighboring GO sheets. After conjunction with Ca^{2+}, the mechanical properties of GO were enhanced to overcome wrinkling; hence, Ca^{2+}-modified GO displayed higher stiffness than the unmodified GO [33]. The FTIR spectrum of the fluorapatite crystal layer coated with GO-chitosan film exhibited a lower-intensity C═O stretching band and higher-intensity carboxy C–O stretching band, demonstrating the cross-links between carboxylic acid in GO and Ca^{2+} (Fig. 4E) [66].

Antibacterial adhesion is one of the antibacterial properties. Bacteria should first adhere to pellicle on the tooth/restoration surface and then accumulate to generate dental plaque for recurrent caries. It is therefore essential to synthesize restorative materials with the ability of antibacterial adhesion. The CFU is the gold standard method to estimate the number of viable bacteria cells in a sample in microbiology [67]. It has two advantages, namely, the capacity for counts of any number of bacteria using dilutions or concentrations, and the exclusion of dead

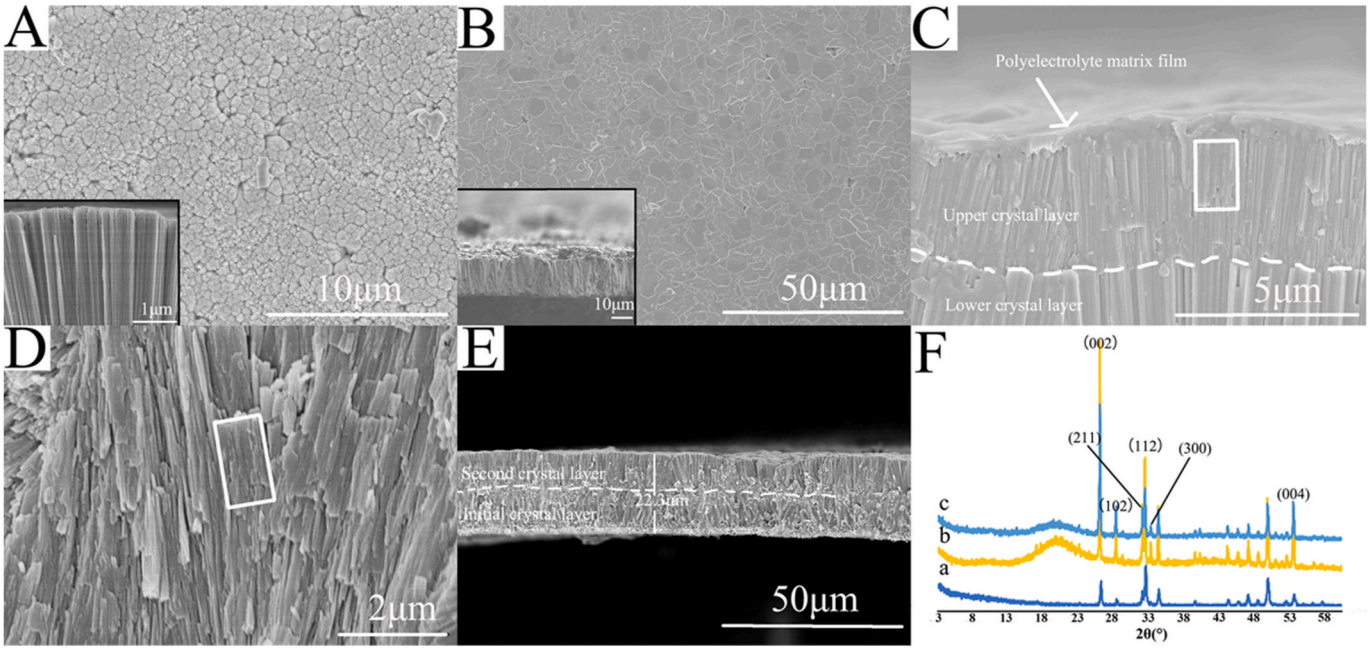

Fig. 5. (A) Top-view of the scanning electron microscopy (SEM) image of the fluorapatite layer consisting of spear-like crystals synthesized with the addition of ethylenediaminetetraacetic acid (EDTA) (the inset is the transversal micrograph). (B) Top-view SEM micrograph of the fluorapatite layer consisting of hexagonal crystals synthesized without the addition of EDTA (the inset is the transversal micrograph). (C) SEM image of the biomaterial coated with a polyelectrolyte matrix film (the arrow represents the polyelectrolyte matrix film and the rectangle represents the prismatic structure). (D) SEM image of native enamel (the rectangle represents the prismatic structure). (E) Transversal-view of the synthesized bioactive material consisting of two fluorapatite crystal layers. (F) X-ray diffraction evaluation (a: native enamel; b: the initial fluorapatite crystal layer; c: the second fluorapatite crystal layer).

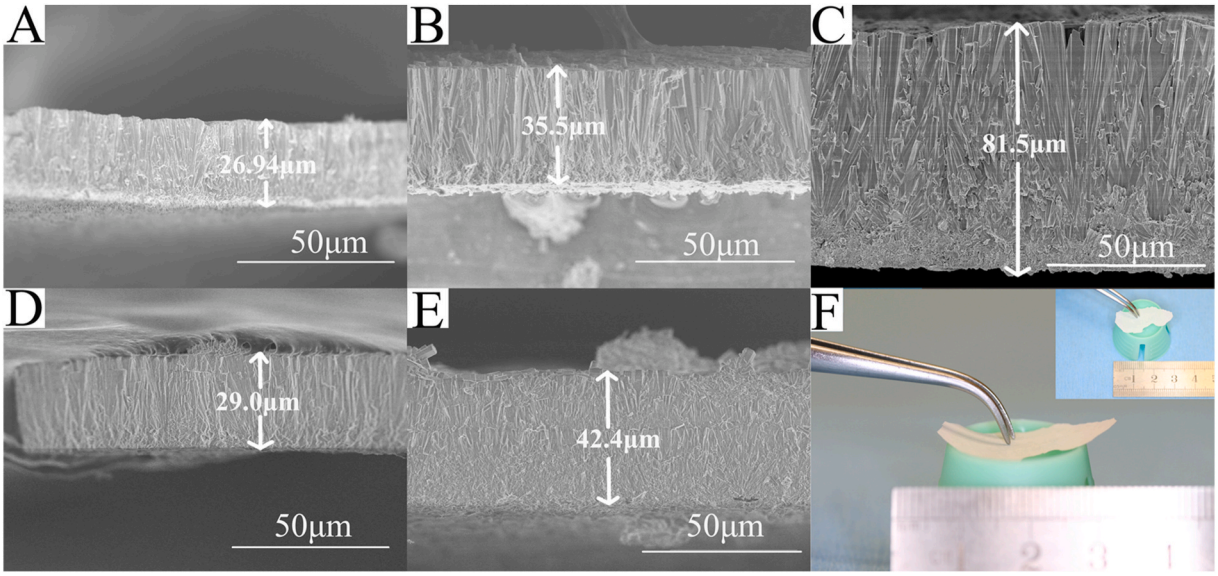

Fig. 6. (A) Scanning electron microscopy (SEM) micrograph of the bioactive material consisting of spear-like crystals synthesized with the addition of ethylenediaminetetraacetic acid (EDTA) after two treatment cycles. (B) SEM image of the bioactive material consisting of spear-like crystals synthesized with EDTA after four treatment cycles. (C) SEM image of the bioactive material consisting of spear-like crystals synthesized with EDTA after eight treatment cycles. (D) SEM image of the synthesized bioactive material consisting of hexagonal crystals synthesized without the addition of EDTA after two treatment cycles. (E) SEM image of the bioactive material consisting of hexagonal crystals synthesized without the addition of EDTA after four treatment cycles. (F) Photograph of the synthesized bioactive material with EDTA after eight treatment cycles.

bacteria and debris [68].

S. mutans is a facultatively anaerobic, gram-positive coccus, which plays a major role in tooth decay because it colonizes onto dental biofilm via cell-to-cell interaction and metabolizes sucrose to lactic acid, and the acidic environment created in the mouth causes demineralization of tooth enamel [69]. The synthesized bioactive material with a GO-chitosan matrix showed inhibitory effects on S. mutans adhesion (Fig. 7). After 24 h' incubation, the quantity of adherent bacteria on the synthesized material with a GO-chitosan matrix ($(25.52 \pm 16.81)*10^4$ CFU/mL) was significantly less than that on the synthesized material with a chitosan-alginate matrix ($(113.60 \pm 107.73)*10^4$ CFU/mL; $p = 0.0063$, *t*-test) and native enamel slices ($(514.00 \pm 276.08)*10^4$

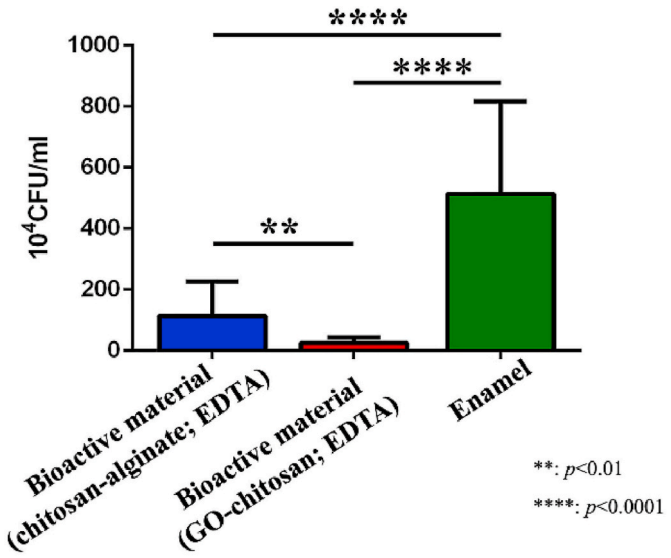

Fig. 7. Colony forming units (CFU) counting evaluation of enamel and synthesized bioactive materials fabricated with eight treatment cycles and different organic matrices after 24 h' incubation.

CFU/mL; $p < 0.0001$, *t*-test). Positively charges residues in chitosan interact with the negatively charged microbial cell membrane, leading to the leakage of proteinaceous and other intracellular constituents [70]. Thus, the synthesized bioactive material with a chitosan-alginate matrix also showed the ability of resisting S. mutans adhesion, compared with native enamel ($p < 0.0001$, *t*-test).

The oral cavity presents a diverse microbial ecosystem; however, the antibacterial model in this study is simple with only one strain of bacteria and 24 h's incubation. Although samples were treated with artificial saliva to mimic the presence of acquired pellicle before S. mutans cells adhesion, caution is needed in extrapolating the results to clinical settings. Further evaluation on more complex models of biofilm formation is required to provide evidence for antibacterial abilities of this synthesized bioactive material.

3.5. Mechanical evaluation

After conjunction with GO, the microhardness of the synthesized bioactive material was substantially enhanced. After three treatment cycles, the Vickers microhardness of the synthesized bioactive material with a GO-chitosan matrix (278.31 ± 45.03) was significantly higher than that with a chitosan-alginate matrix (172.83 ± 32.87; $p = 0.0017$, *t*-test; Fig. 8A). After eight treatment cycles, the Vickers microhardness of the final bioactive material with a GO-chitosan matrix reached the level (464.87 ± 30.75) that is close to the level of native enamel (498.6 ± 19.21; $p = 0.064$, *t*-test; Fig. 8A).

Nanoindentation results demonstrated that there was no significant difference in nanohardness between the synthesized bioactive material with a GO-chitosan matrix (3.29 ± 0.22 GPa) and native enamel (3.54 ± 0.18 GPa ; $p = 0.0764$, *t*-test; Fig. 8B). The nanohardness of the synthesized biomaterial (3.29 ± 0.22 GPa; $p < 0.0001$, *t*-test) and native enamel (3.54 ± 0.18 GPa ; $p < 0.0001$, *t*-test) were both significantly higher than that of acid-etched enamel (0.34 ± 0.03 GPa; Fig. 8B).

Because of the higher organic content, the final bioactive material exhibited higher flexibility than native enamel (Fig. 6F). The TGA data showed that the mass fractions of organic contents and water, and inorganic contents in the fabricated biomaterial were 5.6% and 94.4%, respectively, which was higher than those in human enamel (organics and water: 3.2%; inorganics: 96.8%) (Fig. 8C and D). Therefore, the elastic modulus of the bioactive material synthesized with a GO-chitosan matrix (83.41 ± 10.34 GPa) was significantly higher than that of native enamel (67.09 ± 3.15 GPa ; $p = 0.007$, *t*-test) (Fig. 8B).

The final bioactive material owns similar chemical components and mechanical properties as the native enamel. It is highly resembling enamel structure yet identical. Enamel's unique microstructure is constituted of aligned prisms or rods, running approximately perpendicular from the dentine-enamel junction towards the tooth surface. The ideal structure of these rods is keyhole-like, presenting in a "fish-scale" pattern. The keyhole-like structure further improves enamel's mechanical properties through their interlocking connection [71]. This fish-scale pattern was not achieved in this study.

The process regarding the fabrication of this bioactive material is easy to be scaled-up. Plenty of bioactive materials can be synthesized at the same time. The thickness of native enamel is approximately 0.5–2.5 mm. To achieve similar thickness efficiently for clinical application, the hot-pressing technique [72] can be considered to stack several synthesized bioactive materials together. The computer-aided design/-computer-aided manufacturing (CAD/CAM) technique can then be applied to form the exact morphology and size of the restoration needed. Our bioactive material owns a definite flexibility due to the existence of organic matrixes. It could also be synthesized on a curved surface.

3.6. Cell viability and proliferation

A CCK-8 assay was performed after 7 days' cell culturing to detect the cell viability of samples. Neither the synthesized bioactive material with a GO-chitosan matrix (68.47 ± 14.46; $p = 0.217$, *t*-test) nor with a chitosan-alginate matrix (62.63 ± 14.65; $p = 0.114$, *t*-test) showed a significant difference in cell viability with native enamel (80.71 ± 14.17) (Supplementary Fig. 3A). Cells proliferated on the surface of the synthesized bioactive materials and native enamel after 7 days of culturing were illustrated on Supplementary Figs. 3B and C. Besides, the –COOH in GO chelates with free calcium ions to trigger the heterogeneous nucleation by the electrostatic interaction, which may prevent the release of free GO [27]. The biosafety of our synthesized material was therefore confirmed.

3.7. MD simulations of the mineralization process

MD simulations can be useful for gaining a fundamental understanding of reaction mechanisms [73], and, in particular, crystallization kinetics on an atomic and molecular level [74]. In the present study, we introduced EDTA, adjusted the pH value, and varied mineralization microenvironment to regulate crystal growth and assembly to mimic the properties of native enamel. This is the first MD simulations to study the full atomic behaviors of crystallization process when looking into the effects of variables on the crystallization mechanism. Our results provide a solid theoretical foundation for further investigations of biomimetic mineralization in dental materials.

Mediating effect of EDTA on crystal growth. EDTA is a chelating agent, which has different forms with different chelating abilities depending on the pH value. Previous studies demonstrated that EDTA mediates crystal growth by chelating Ca^{2+} and controlling its release [28]. This is consistent with the results of our study. After the introduction of EDTA, the crystal morphology changed from hexagonal to a spear-like shape, and the size decreased from the micro-to nanoscale (Fig. 2B and C).

At pH 5.5, EDTA has four carboxyl groups to chelate Ca^{2+} ions, and can act as a 'bridge' to connect two neighboring Ca^{2+} ions to form a Ca–EDTA complex (Supplementary Fig. 4A). After the addition of EDTA, the majority of Ca^{2+} ions were chelated. Moreover, ion aggregation was slower than that in the solution without EDTA (Supplementary Fig. 5A), and CaP nucleated with a smaller size for the same duration of MD simulations (Supplementary Fig. 5B). Although the number of EDTA molecules (10) added to the system was not large, the difference in binding energy was sufficient to demonstrate the decrease in aggregation speed caused by EDTA. The differences in ion bonding energy (Supplementary Fig. 6A) showed that the ion interaction in the solution

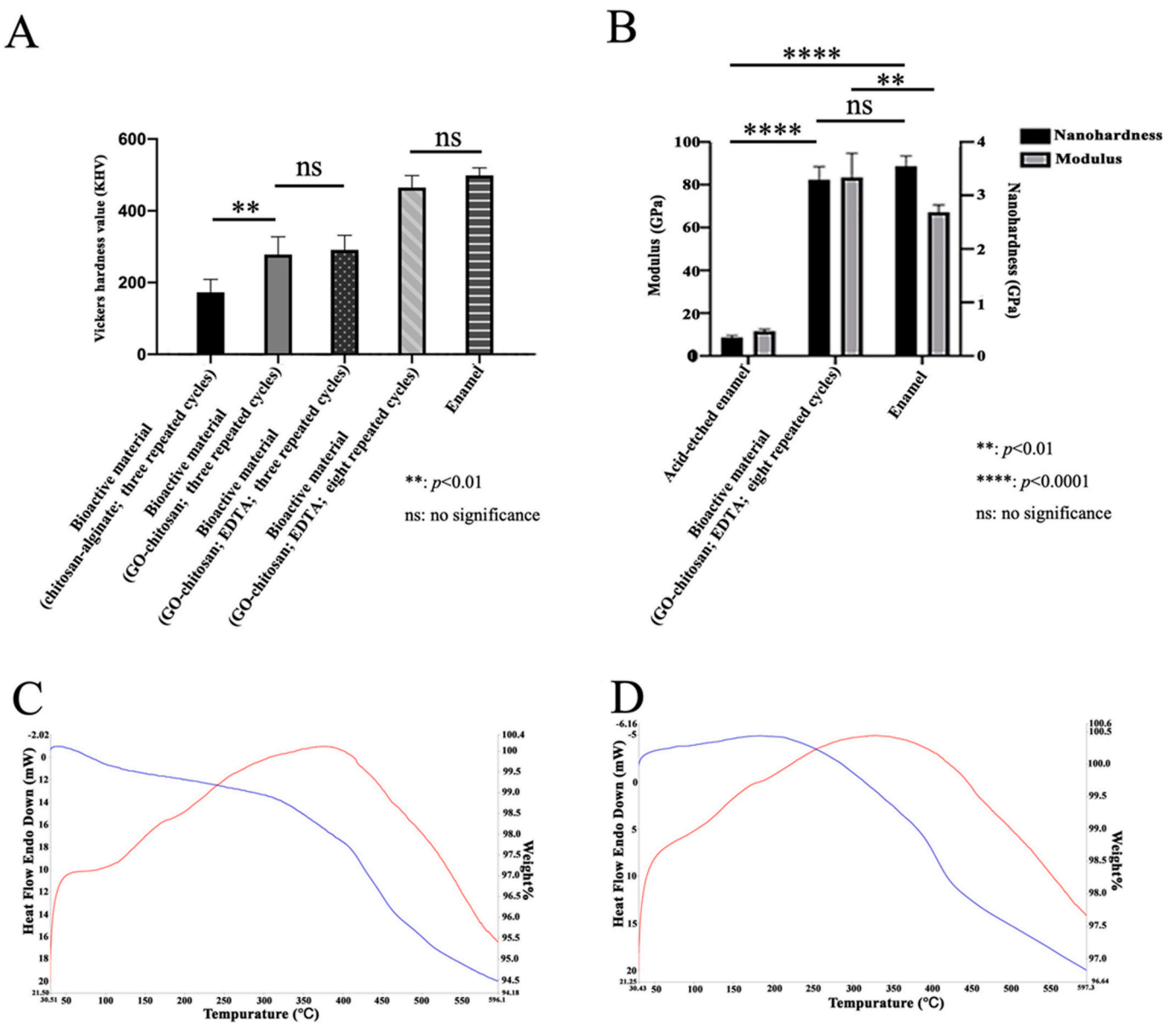

Fig. 8. Mechanical evaluation. (A) Vickers hardness value of enamel and bioactive materials fabricated with different treatment cycles and organic matrices. (B) Elastic modulus and nanohardness of acid-etched enamel, enamel, and the final bioactive material. (C, D) Thermogravimetric analysis (TGA) results of the final bioactive material and enamel, respectively.

was weaker in the presence of EDTA. Thus, EDTA decreases the free energy of the metastable mineralization solution, resulting in the observed slow ion aggregation. With the steady and continuous release of Ca^{2+} ions from Ca–EDTA complexes, only single nanorods formed from each nucleate [75]; meanwhile, fast growth in the crystal polar (001) direction [28] and diffusion-limited growth resulted in the formation of spear-like crystals with one sharp end, which is consistent with the SEM observations in Fig. 2B. In the solution without EDTA, owing to the rapid consumption of free ions in the initial stages, crystal growth quickly ceased, leading to the formation of large (microscale) crystals.

EDTA could regulate the crystal size and morphology for the formation of enamel-like crystals. After the introduction of EDTA, the cross-section diameter of formed crystals decreased from the micro-to nanoscale. The obtained bioactive material composed of nanoscaled crystals has a smoother appearance than that composed of microscaled crystals.

The introduction of EDTA caused changes in the crystal morphology and size; however, no difference in mechanical property was detected. After three treatment cycles, the Vickers microhardness of the biomaterial fabricated with EDTA (291.30 ± 36.93) was not statistically different from that fabricated without EDTA (278.31 ± 45.03, $p = 0.629$, *t*-test; Fig. 8A).

Influence of pH *value on crystal growth.* At pH 4.5, nanoscale fluorapatite crystals with a spherical morphology formed (Supplementary Fig. 7A), which parallelly aggregated and assembled into prismatic microstructures (Supplementary Fig. 8B). At $2\theta = 28.1$, the diffraction peak of the fluorapatite nanospheres was distinct, demonstrating the preferred orientation on the (102) plane (Supplementary Fig. 7F). By contrast, at pH 5.5, hexagonal fluorapatite crystals formed, which showed a preferred orientation on the (002) plane (Fig. 5F).

The MD simulations indicated that the electrostatic interaction at pH 5.5 was stronger than that at pH 4.5 (Supplementary Fig. 6B). Moreover, ion aggregation was faster and CaP nucleates were larger at pH 5.5 (Supplementary Fig. 5A). This arose because of rapid ion consumption at the beginning of the simulation, resulting in the quick cessation of crystal growth and a large crystal size. This is consistent with the SEM

observation of microscale crystals that formed at pH 5.5 (Fig. 2F). When the solution was more acidic (at pH 4.5), the electrostatic interactions between ions were weaker, which may keep calcium and phosphate in an ion phase instead of precipitating. Therefore, ion aggregation was slower and CaP nucleates were smaller at pH 4.5 (Supplementary Fig. 5C), and the fluorapatite crystals formed were nanoscale in size (Supplementary Fig. 8A).

In addition, because of the pKa value of phosphate, the pH value could change the protonation state of PO_4, and lead to different calcium coordination behavior and ion aggregation. The dominant phosphate groups at pH 4.5 and 5.5 are $H_2PO_4^-$ and HPO_4^{2-} ions, respectively. A HPO_4^{2-} ion has one more 'naked' oxygen than that of a $H_2PO_4^-$ ion; hence, HPO_4^{2-} ions have a stronger coordination bond with Ca^{2+} ions. Thus, it was observed that ions aggregated more tightly at pH 5.5 than at pH 4.5. In a $H_2PO_4^-$ ion, only one 'naked' oxygen coordinately binds with the Ca^{2+} ion; the remaining OH^- radicals hydrogen-bond with H_2O (Supplementary Fig. 4B). Thus, both the calcium coordination interaction and hydrogen bonding were involved in ion aggregation at pH 4.5. However, at pH 5.5, ion aggregation was dominated by the calcium coordination interaction (Supplementary Fig. 4C). Coordination interactions are stronger than hydrogen bonds and can cause different crystal assemblies; hence, different crystal morphologies and orientations were observed at different pH values. Spherical and hexagonal crystals separately formed at pH 4.5 and 5.5, and showed an orientation on the (102) plane and (002) plane, respectively.

Influence of mineralization microenvironment on crystal growth. During oven heating, both the upper and lower surfaces of the mineralization base were fully mineralized. The crystal grown on the different surfaces had different morphologies and orientations, resulting in different interior structures in the fluorapatite biomaterial. The biomaterial fabricated on the bottom surface of the mineralization base had a continuous profile with minimal structural defects and high orientation preference (Fig. 5E); by contrast, the biomaterial on the top surface lacked prism-like forms and an orderly orientation (Supplementary Fig. 8). Such a distinct difference was caused by the different mineralization microenvironments. This open system led to a fast loss of HCl and H_2O molecules during heating. This may have caused the solution above the mineralization base to have a higher ion concentration and higher pH value than the solution below the mineralization base. A high pH value and ion concentration accelerate crystal growth. Therefore, the experimentally observed growth rate on the top surface was faster than that on the bottom surface.

To further investigate the influence of the mineralization microenvironment, we ran MD simulations at high and low ion concentrations at pH 5.5. The change in binding energy during the simulation showed that the electrostatic interactions between ions in the concentrated solution were stronger than those in the low-concentration solution (Supplementary Fig. 6C). These stronger electrostatic interactions led to ion aggregation taking place over a short period of time, resulting in fast mineralization. Thus, the thickness of the biomaterial fabricated on the top surface was larger than that fabricated on the bottom surface.

The mineralization microenvironment above the base not only had a high ion concentration, but also a high pH value, caused by the rapid vaporization of HCl and H_2O. Previous studies demonstrated that OH^- could regulate crystal growth by triggering the active sites at crystal facets [76]. Specifically, the pH controls whether crystal growth is determined by the crystal's interior structure or by the exterior mineralization condition. When the pH value is high (>7), the exterior mineralization conditions dominate. At a higher OH^- concentration, each crystal facet generates more active sites [76]. The MD simulations show that extra OH^- ions not only coordinate to the calcium sites on the crystal facet, but also to the phosphate sites by hydrogen bonding (Supplementary Fig. 4D). This results in a larger number of active sites on the facet and, ultimately, branched crystal structures [75]. In addition, after the addition of extra OH^- ions, ion aggregation became faster, and more active sites were generated at crystal facets leading to the formation of CaP clusters with 'tentacles' (Supplementary Fig. 5D). This might result in crystals with small branches at their ends (Supplementary Figs. 8A and C), which is corresponding to the results from a previous study [76]. Since the MD simulation modeling described a very small volume of extra OH^- ions in a very limited timescale in comparison to real-world process, further evidence is needed from laboratory experiments.

The mineralization environment below the base was more stable than that above the base, and had a lower pH value; thus, the crystal growth was mainly affected by its interior structure instead of the exterior condition. At a lower pH value, free Ca^{2+} ions were incorporated into the crystal lattice and crystallites grew anisotropically [76]. Consequently, each nucleate grew into an individual crystal and the spear-like crystal was obtained (Fig. 2B) [75,77]. However, the strong absorption of the extra OH^- ions at the high pH 11 resulted in each facet having almost the same probability of generating active sites [76,77]. Under these conditions, more active sites were produced and more Ca ions combined with the active sites of the crystallite. Thus, the morphology of the crystal at the top surface had a flower-like form with small branches at its end.

The mineralization microenvironment also affects the mechanical properties. We found that after three treatment cycles, the Vickers microhardness of the biomaterial fabricated on the top surface of the mineralization base (179.08 ± 38.11) was significantly lower than that fabricated on its bottom surface (278.31 ± 45.03, $p = 0.0001$, *t*-test; Supplementary Fig. 9). Based on SEM evaluation, the biomaterial fabricated on the top surface had a looser internal structure and poorer microhardness than that fabricated on the bottom surface owing to the disorderly arranged fluorapatite crystals (Supplementary Fig. 8).

4. Conclusion

We have developed an effective acellular method to fabricate an enamel-inspired macroscopic bioactive material. This bioactive material is analogous to the native enamel in chemical components, mechanical properties and crystallographic structure.

Besides, it possesses antibacterial adhesion property and higher elastic modulus that are even superior to enamel, advancing current technology in restorative dentistry. This work combines the experimental investigation and theoretical MD analysis to explore the details of the crystallization process influenced by different variables, providing robust evidence to support the establishment of the non-cell based strategy for the synthesis of enamel-mimetic biomaterials.

Declaration of interests

The authors declare that they have no known competing financial interests or personal relationships that could have appeared to influence the work reported in this paper.

Materials and correspondence

Correspondence to Hai Ming Wong and Quan Li Li.

CRediT authorship contribution statement

Hai Ming Wong: Conceptualization, Methodology, Software, Validation, Formal analysis, Investigation, Resources, Data curation, Writing – original draft, Writing – review & editing, Visualization, Supervision, Project administration, Funding acquisition. **Yu Yuan Zhang:** Conceptualization, Methodology, Software, Validation, Formal analysis, Investigation, Resources, Data curation, Writing – original draft, Writing – review & editing, Visualization. **Quan Li Li:** Conceptualization, Methodology, Investigation, Resources, Data curation, Writing – review & editing, Visualization, Supervision, Project administration, Funding acquisition.

Acknowledgement

The work described in this paper was fully supported by a grant from the NSFC/RGC Joint Research Scheme sponsored by the Research Grants Council of the Hong Kong Special Administrative Region, China and the National Natural Science Foundation of China (Project No. N-HKU706/20).

Appendix A. Supplementary data

Supplementary data to this article can be found online at https://doi.org/10.1016/j.bioactmat.2021.05.035.

Data availability

All of the data reported in this work as available upon request.

References

[1] C. Du, G. Falini, S. Fermani, C. Abbott, J. Moradian-Oldak, Supramolecular assembly of amelogenin nanospheres into birefringent microribbons, Science 307 (2005) 1450–1454.
[2] J.W. Dunlop, P. Fratzl, Biological composites, Annu. Rev. Mater. Res. 40 (2010) 1–24.
[3] J. Aizenberg, P. Fratzl, Biological and biomimetic materials, Adv. Mater. 21 (2009) 387–388.
[4] Z. Zou, et al., Dental enamel-like hydroxyapatite transformed directly from monetite, J. Mater. Chem. 22 (2012) 22637–22641.
[5] N. Zhou, et al., Oral health status of children and adolescents with intellectual disabilities: a systematic review and meta-analysis, Dev. Med. Child Neurol. 59 (2017) 1019–1026.
[6] C.A. Carrera, et al., The use of micro-CT with image segmentation to quantify leakage in dental restorations, Dent. Mater. 31 (2015) 382–390.
[7] G. Derchi, M. Vano, A. Barone, U. Covani, A. Diaspro, M. Salerno, Bacterial adhesion on direct and indirect dental restorative composite resins: an in vitro study on a natural biofilm, J. Prosthet. Dent 117 (2017) 669–676.
[8] H.M. Wong, et al., Validation of the Hong Kong oral health literacy assessment task for paediatric dentistry (HKOHLAT-P), Int. J. Paediatr. Dent. 23 (2013) 366–375.
[9] N. Beyth, A.J. Domb, E.I. Weiss, An in vitro quantitative antibacterial analysis of amalgam and composite resins, J. Dent. 35 (2007) 201–206.
[10] L.C. Palmer, et al., Biomimetic systems for hydroxyapatite mineralization inspired by bone and enamel, Chem. Rev. 108 (2008) 4754–4783.
[11] F. Carella, L. Degli Esposti, D. Barreca, G.A. Rizzi, G. Martra, P. Ivanchenko, G. E. Casado, J.G. Morales, J.M.D. Lòpez, A. Tampieri, M. Iafisco, Role of citrate in the formation of enamel-like calcium phosphate oriented nanorod arrays, CrystEngComm 21 (2019) 4684–4689.
[12] Y. Yin, et al., Chemical regeneration of human tooth enamel under near-physiological conditions, Chem. Commun. (2009) 5892–5894.
[13] C. Shao, et al., Repair of tooth enamel by a biomimetic mineralization frontier ensuring epitaxial growth, Sci Adv 5 (2019) 9569.
[14] S. Busch, Regeneration of human tooth enamel, Angew. Chem. Int. Ed. 43 (2004) 1428–1431.
[15] J. Takagi, Structural basis for ligand recognition by RGD (Arg-Gly-Asp)-dependent integrins, Biochem. Soc. Trans. (2004) 403–406.
[16] Y. Cao, et al., Agarose hydrogel biomimetic mineralization model for the regeneration of enamel prismlike tissue, ACS Appl. Mater. Interfaces 6 (2013) 410–420.
[17] Z. Huang, et al., Bioactive nanofibers instruct cells to proliferate and differentiate during enamel regeneration, J. Bone Miner. Res. 23 (2008) 1995–2006.
[18] Y. Fan, Z. Sun, J. Moradian-Oldak, Controlled remineralization of enamel in the presence of amelogenin and fluoride, Biomaterials 30 (2009) 478–483.
[19] Q. Ruan, et al., An amelogenin–chitosan matrix promotes assembly of an enamel-like layer with a dense interface, Acta Biomater. 9 (2013) 7289–7297.
[20] S. Elsharkawy, et al., Protein disorder–order interplay to guide the growth of hierarchical mineralized structures, Nat. Commun. 9 (2018) 2145.
[21] B. Yeom, et al., Abiotic tooth enamel, Nature 543 (2017) 95.
[22] K. Aita, Y. Oaki, C. Ohtsuki, H. Imai, Fabrication of self-standing films consisting of enamel-like oriented nanorods using artificial peptide, CrystEngComm 17 (2015) 5551–5555.
[23] S. Imazato, T. Imai, R.R.B. Russell, M. Torii, S. Ebisu, Antibacterial activity of cured dental resin incorporating the antibacterial monomer MDPB and an adhesion-promoting monomer, J. Biomed. Mater. Res. 39 (1998) 511–515.
[24] G. Marczuk-Kolada, P. Jakoniuk, J. Mystkowska, E. Łuczaj-Cepowicz, D. Waszkiel, J.R. Dabrowski, K. Leszczyńska, Fluoride release and antibacterial activity of selected dental materials, Postepy Hig. Med. Dosw. 60 (2006) 416–420.
[25] Y. Zhang, et al., Facile preparation, optical and electrochemical properties of layer-by-layer V2O5 quadrate structures, Appl. Surf. Sci. 399 (2017) 151–159.
[26] M. Lin, et al., Facial layer-by-layer engineering of upconversion nanoparticles for gene delivery: near-infrared-initiated fluorescence resonance energy transfer tracking and overcoming drug resistance in ovarian cancer, ACS Appl. Mater. Interfaces 9 (2017) 7941–7949.
[27] Wang, et al., Rapid regeneration of enamel-like-oriented inorganic crystals by using rotary evaporation, Mater. Sci. Eng. C 115 (2020) (2020), 111141.
[28] J. Liu, et al., Self-assembly of hydroxyapatite nanostructures by microwave irradiation, Nanotechnology 16 (2004) 82.
[29] S. Liu, et al., Antibacterial activity of graphite, graphite oxide, graphene oxide, and reduced graphene oxide: membrane and oxidative stress, ACS Nano 5 (2011) 6971–6980.
[30] K. Yang, et al., Graphene in mice: ultrahigh in vivo tumor uptake and efficient photothermal therapy, Nano Lett. 10 (2010) 3318–3323.
[31] H. Liu, et al., Simultaneous reduction and surface functionalization of graphene oxide for hydroxyapatite mineralization, J. Phys. Chem. B 116 (2012) 3334–3341.
[32] K. Pajor, L. Pajchel, J. Kolmas, Hydroxyapatite and fluorapatite in conservative dentistry and oral implantology - a review, Materials 12 (2019) 2683.
[33] Y. Dong, et al., Blue luminescent graphene quantum dots and graphene oxide prepared by tuning the carbonization degree of citric acid, Carbon 50 (2012) 4738–4743.
[34] M.J. Frisch, et al., Gaussian 03, gaussian, Pittsburgh PA, 2003.
[35] L.P. Wang, et al., Building a more predictive protein force field: a systematic and reproducible route to AMBER-FB15, J. Phys. Chem. B 121 (2017) 4023–4039.
[36] D.A. Case, et al., AMBER16, San Francisco, 2016.
[37] P. Eastman, et al., OpenMM 7: rapid development of high performance algorithms for molecular dynamics, PLoS Comput. Biol. 13 (2017), 1005659.
[38] R.L. Davidchack, R. Handel, M.V. Tretyakov, Langevin thermostat for rigid body dynamics, J. Chem. Phys. 130 (2009) 234101.
[39] H.C. Andersen, Rattle: a "velocity" version of the shake algorithm for molecular dynamics calculations, J. Comput. Phys. 52 (1983) 24–34.
[40] C.I. Bayly, et al., A well-behaved electrostatic potential based method using charge restraints for deriving atomic charges: the RESP model, J. Phys. Chem. 97 (1993) 10269–10280.
[41] J. Wang, et al., Development and testing of a general amber force field, J. Comput. Chem. 25 (2004) 1157–1174.
[42] C.E. Fowler, et al., Influence of surfactant assembly on the formation of calcium phosphate materials—a model for dental enamel formation, J. Mater. Chem. 15 (2005) 3317–3325.
[43] C. Robinson, S. Connell, J. Kirkham, S.J. Brookes, R.C. Shore, A.M. Smith, The effect of fluoride on the developing tooth, Caries Res. 38 (2004) 268–276.
[44] M.G. Sankalia, et al., Reversed chitosan–alginate polyelectrolyte complex for stability improvement of alpha-amylase: optimization and physicochemical characterization, Eur. J. Pharm. Biopharm. 65 (2007) 215–232.
[45] R.S. Lacruz, S. Habelitz, J.T. Wright, M.L. Paine, Dental enamel formation and implications for oral health and disease, Physiol. Rev. 97 (2017) 939–993.
[46] J. Moradian-Oldak, Protein-mediated enamel mineralization, Front. Biosci. Landmark Ed. 17 (2012) 1996–2023.
[47] S.I. Stupp, P.V. Braun, Molecular manipulation of microstructures: biomaterials, ceramics, and semiconductors, Science 277 (1997) 1242–1248.
[48] C. Sartori, et al., Determination of the cation content of alginate thin films by FTIR spectroscopy, Polymer 38 (1997) 43–51.
[49] T. Li, et al., Quaternized chitosan/alginate nanoparticles for protein delivery, J. Biomed. Mater. Res. A. 83 (2007) 383–390.
[50] P. Li, et al., Chitosan-alginate nanoparticles as a novel drug delivery system for nifedipine, Int. J. Biomed. Sci.: IJBS. 4 (2008) 221.
[51] Z. Li, et al., Chitosan–alginate hybrid scaffolds for bone tissue engineering, Biomaterials 26 (2005) 3919–3928.
[52] H.L. Gao, et al., Mass production of bulk artificial nacre with excellent mechanical properties, Nat. Commun. 8 (2017) 287.
[53] M. Dash, et al., Ulvan-chitosan polyelectrolyte complexes as matrices for enzyme induced biomimetic mineralization, Carbohydr. Polym. 182 (2018) 254–264.
[54] Y. Qi, et al., Effects of molecular weight and concentration of poly (acrylic acid) on biomimetic mineralization of collagen, ACS Biomater. Sci. Eng. 4 (2018) 2758–2766.
[55] H.F. Chen, et al., Acellular synthesis of a human enamel-like microstructure, Adv. Mater. 18 (2006) 1846–1851.
[56] E. Mohammadi, et al., Dynamic-template-directed multiscale assembly for large-area coating of highly-aligned conjugated polymer thin films, Nat. Commun. 8 (2017) 16070.
[57] Y.F. Wang, H. Iino, J.I. Hanna, Planar-orientation polycrystalline thin film of liquid-crystalline organic semiconductor by template-directed self-assembly, APEX 10 (2017), 101601.
[58] I.R. Nizameev, et al., Surfactant templated oriented 1-D nanoscale platinum and palladium systems on a modified silicon surface, Nano-Structures and Nano-Objects 17 (2019) 1–6.
[59] H. Lee, et al., Mussel-inspired surface chemistry for multifunctional coatings, Science 318 (2007) 426–430.
[60] Y.Z. Zhou, et al., Polydopamine-induced tooth remineralization, ACS Appl. Mater. Interfaces 4 (2012) 6901–6910.
[61] Z. Lin, et al., Solvent-assisted thermal reduction of graphite oxide, J. Phys. Chem. C 114 (2010) 14819–14825.
[62] Y. Lin, J. Jin, M. Song, Preparation and characterisation of covalent polymer functionalized graphene oxide, J. Mater. Chem. 21 (2011) 3455–3461.
[63] A.M. Dimiev, J.M. Tour, Mechanism of graphene oxide formation, ACS Nano 8 (2014) 3060–3068.
[64] Q. Yang, et al., Covalent functionalization of graphene with polysaccharides, Ind. Eng. Chem. Res. 51 (2011) 310–317.

[65] J. Bao, et al., An array of concentric composite nanostructure of metal nanowires encapsulated in zirconia nanotubes: preparation, characterization, and magnetic properties, Chem. Mater. 14 (2002) 4709–4713.
[66] Á. Serrano-Aroca, L. Iskandar, S. Deb, Green synthetic routes to alginate-graphene oxide composite hydrogels with enhanced physical properties for bioengineering applications, Eur. Polym. J. 103 (2018) 198–206.
[67] J.H. Miller, Determination of viable cell counts: bacterial growth curves, Experiments in Molecular Genetics 31 (1972) 36.
[68] R. Hazan, Y.A. Que, D. Maura, L.G. Rahme, A method for high throughput determination of viable bacteria cell counts in 96-well plates, BMC Microbiol. 12 (2012) 1–7.
[69] M.E. Davey, G.A. O'toole, Microbial biofilms: from ecology to molecular genetics, Microbiol. Mol. Biol. Rev. 64 (2000) 847–867.
[70] L.E.C. Depaz, A. Resin, K.A. Howard, D.S. Sutherland, P.L. Wejse, Antimicrobial effect of chitosan nanoparticles on streptococcus mutans biofilms, Appl. Environ. Microbiol. 77 (2011) 3892–3895.
[71] S. Habelitz, S.J. Marshall, G.W. Marshall Jr., M. Balooch, Mechanical properties of human dental enamel on the nanometre scale, Arch. Oral Biol. 46 (2001) 173–183.
[72] L.B. Mao, et al., Synthetic nacre by predesigned matrix-directed mineralization, Science 354 (2016) 107–110.
[73] W. Zhao, et al., Predicting the structure–activity relationship of hydroxyapatite-binding peptides by enhanced-sampling molecular simulation, Langmuir 32 (2016) 7009–7022.
[74] J.W. Shen, et al., Molecular simulation of protein adsorption and desorption on hydroxyapatite surfaces, Biomaterials 29 (2008) 513–532.
[75] Z.L. Wang, X.Y. Kong, J.M. Zuo, Induced growth of asymmetric nanocantilever arrays on polar surfaces, Phys. Rev. Lett. 91 (2003), 185502.
[76] R.C. Wang, et al., ZnO hexagonal arrays of nanowires grown on nanorods, Appl. Phys. Lett. 86 (2005), 251104.
[77] L.M. Sander, Diffusion-limited aggregation: a kinetic critical phenomenon? Contemp. Phys. 41 (2000) 203–218.